Engineering Geology 301 (2022) 106613

Contents lists available at ScienceDirect

Engineering Geology

journal homepage: www.elsevier.com/locate/enggeo

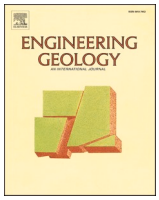

Application of petrophysical relationships to electrical resistivity models for assessing the stability of a landslide in British Columbia, Canada

Jessica Holmes [a,b,*,1], Jonathan Chambers [b], Paul Wilkinson [b], Philip Meldrum [b], Mihai Cimpoiașu [b], James Boyd [b,c], David Huntley [d], Paul Williamson [b], David Gunn [b], Ben Dashwood [b], Jim Whiteley [b], Arnaud Watlet [b], Matthew Kirkham [b], Kelvin Sattler [e], David Elwood [e], Vinayagamoothy Sivakumar [f], Shane Donohue [g]

[a] Newcastle University, Newcastle, United Kingdom
[b] British Geological Survey, Nottingham, United Kingdom
[c] Lancaster University, Lancaster, United Kingdom
[d] Geological Survey of Canada, Vancouver, British Columbia, Canada
[e] University of Saskatchewan, Saskatoon, Saskatchewan, Canada
[f] Queen's University Belfast, Belfast, United Kingdom
[g] University College Dublin, Dublin, Ireland

ARTICLE INFO

Keywords:
Electrical resistivity tomography
Geophysical monitoring
Landslides
Hydrogeophysics

ABSTRACT

Landslides in the Thompson River Valley, British Columbia, Canada, threaten the serviceability of two railway lines that connect Vancouver to the rest of Canada and the US. To minimise the impact of slope instability on vital transport infrastructure, as well as on terrestrial and aquatic ecosystems, public safety, communities, local heritage, and the economy, and to better inform decision making, there is a need for monitoring. Since 2013, the Ripley Landslide – a small, slow-moving, translational landslide – has been the focus of monitoring efforts in the Thompson River Valley transportation corridor. In November 2017, a novel Electrical Resistivity Tomography (ERT) monitoring system was installed on the site, providing near-real-time data collection via a telemetric link. 4-Dimensional resistivity models are presented in the context of moisture content and soil suction, two parameters known to influence slope stability in the Thompson River Valley. Here, we discuss the development of laboratory-based petrophysical relationships that relate electrical resistivity to moisture content and soil suction directly, building on relationships developed in the field. The 4-D ERT models were calibrated using these petrophysical relationships to provide insights into the complex spatial and temporal variations in moisture content and soil suction. This study highlights the utility of geoelectrical monitoring for assessing slope stability in the context of moisture-driven landslides.

1. Introduction

Demand placed on the global transport network continues to increase in response to population growth, with many networks already operating at, or exceeding, capacity (Hugenschmidt, 2010). Combined with additional challenges posed by environmental change (IPCC, 2014), this means that landslides on the transport network are increasing in frequency. Slope failures proximal to transport infrastructure have the potential to disrupt rail and road travel and are potentially hazardous to the people using the transport networks (Smethurst et al., 2017), and cause significant impact to the economy (Dijkstra et al., 2014; Glendinning et al., 2014). Furthermore, given that emergency repair works cost ten times as much as planned maintenance works (Glendinning et al., 2005), there is significant stakeholder interest in monitoring slopes affecting transport infrastructure (Mattsson and Jenelius, 2015).

Near-surface geophysical techniques provide an opportunity to acquire information about large volumes of the subsurface, relatively inexpensively, and more quickly than traditional visual surveys and geotechnical investigations can provide. Indeed, Electrical Resistivity

* Corresponding author at: Newcastle University, Newcastle, United Kingdom.
E-mail address: jessica.holmes@newcastle.ac.uk (J. Holmes).
[1] Previously: Queen's University Belfast, Belfast, United Kingdom.

https://doi.org/10.1016/j.enggeo.2022.106613
Received 9 July 2021; Received in revised form 16 February 2022; Accepted 8 March 2022
Available online 11 March 2022

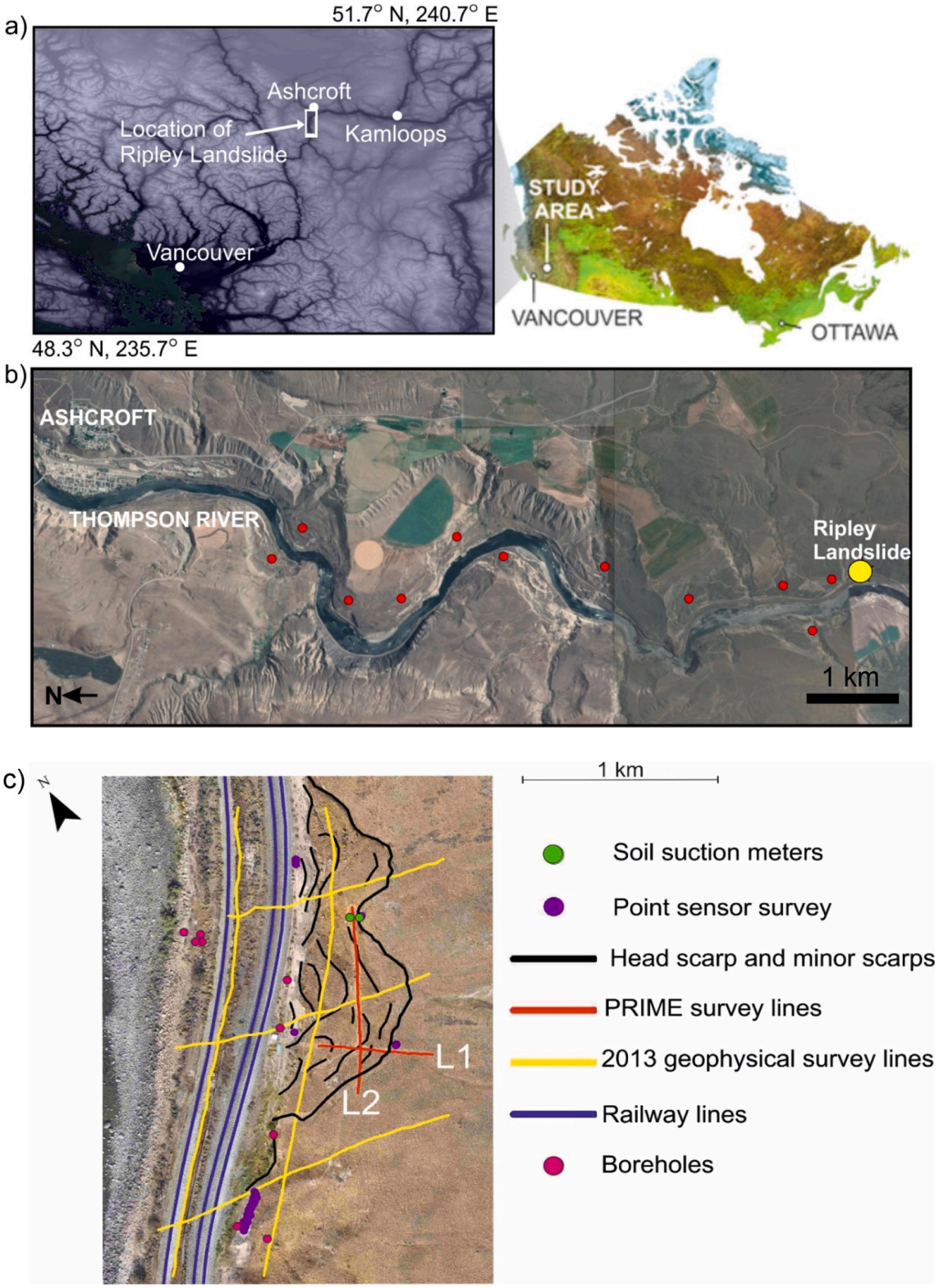

Fig. 1. a) Location of the Thompson River valley area of interest (white rectangle). b) Thompson River Valley, showing locations of landslides (red dots), and the Ripley Landslide (yellow dot). c) Location of PRIME arrays (Line 1 (L1) and Line 2 (L2)), 2013 reconnaissance surveys, and other monitoring equipment. The location of the railway lines is also highlighted. Image BGS©UKRI, ©Google Earth, contains ©Geological Survey of Canada data. (For interpretation of the references to colour in this figure legend, the reader is referred to the web version of this article.)

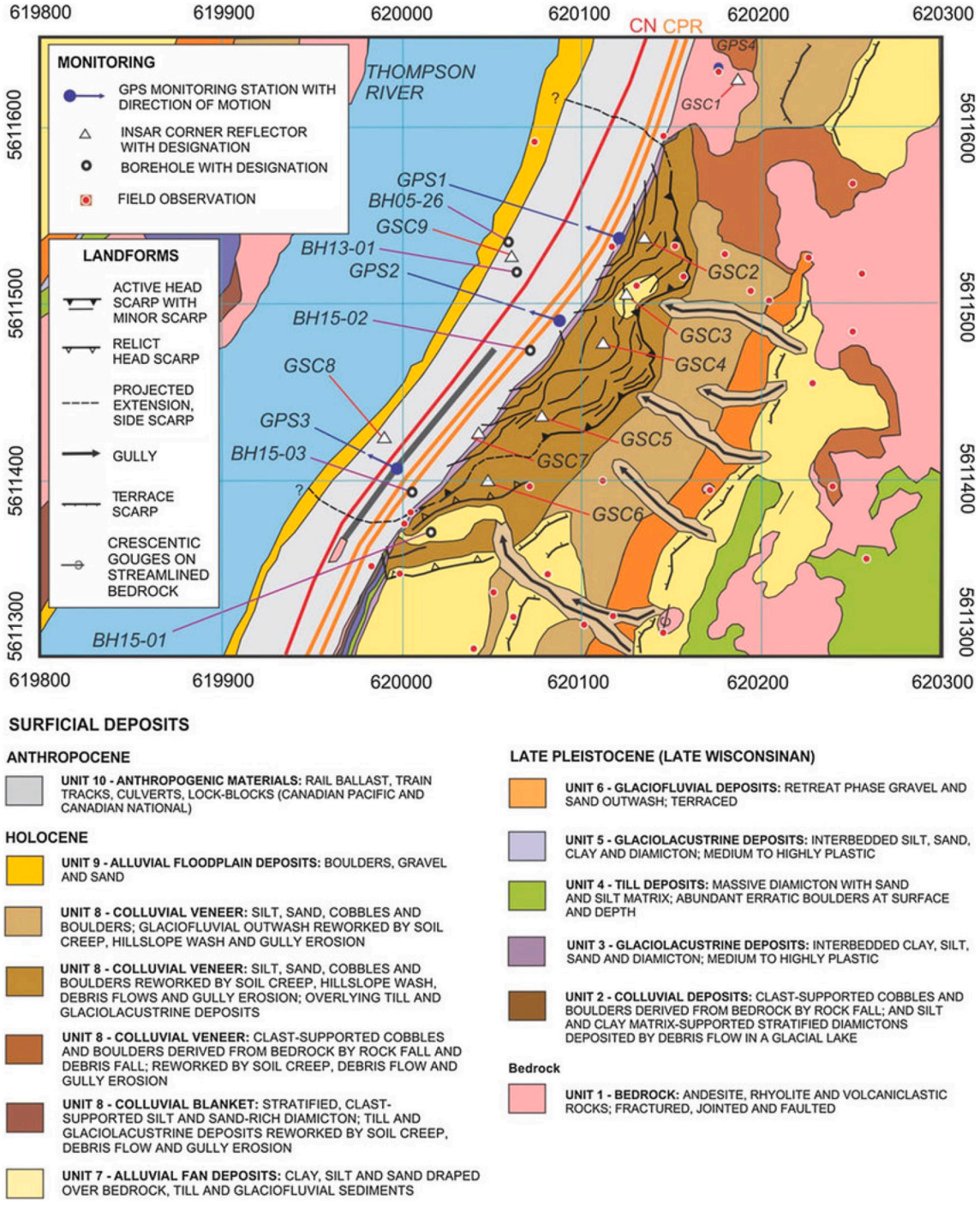

Fig. 2. Geological map of the Ripley Landslide (after Huntley and Bobrowsky, 2014).

Tomography (ERT) is now increasingly being used for monitoring unstable slopes (Chambers et al., 2014; Perrone et al., 2014; Gunn et al., 2015; Wilkinson et al., 2016; Whiteley et al., 2019; Holmes et al., 2020).

Electrical resistivity is affected by many factors, including lithology, mineralogy, porosity and density of the subsurface. Resistivity is also sensitive to moisture content (Archie, 1942; Waxman and Smits, 1968), changing resistivity of the pore fluid (Archie, 1942; Waxman and Smits, 1968), and temperature (Hayley et al., 2007). Resistivity can therefore be used as a proxy to monitor changes in these parameters over time.

Moisture content is a key control on slope stability (Labuz and Zang, 2012; Yao et al., 2019). Empirical rainfall and snowmelt thresholds have long been used in landslide prediction (Caine, 1980; Guzzetti et al., 2008), and rely on the intrinsic connection between rainfall intensity and duration and the associated changes in moisture content in the subsurface (Francesco et al., 2012). However, even on a local scale, heterogeneities in slope lithology mean that surface measurements of rainfall may be insufficient to predict the location and timing of slope failure; complex hydrogeological pathways present within slopes are critical in determining slope behaviour (Onda et al., 2004; Lehmann et al., 2013; Marino et al., 2020). As moisture content is a factor that affects electrical resistivity, ERT can be used to monitor changes in moisture content in the subsurface through space (Samoüelian et al., 2005) and time (Abdu et al., 2008), and so is a useful tool in slope stability assessment (Lehmann et al., 2013; Uhlemann et al., 2017).

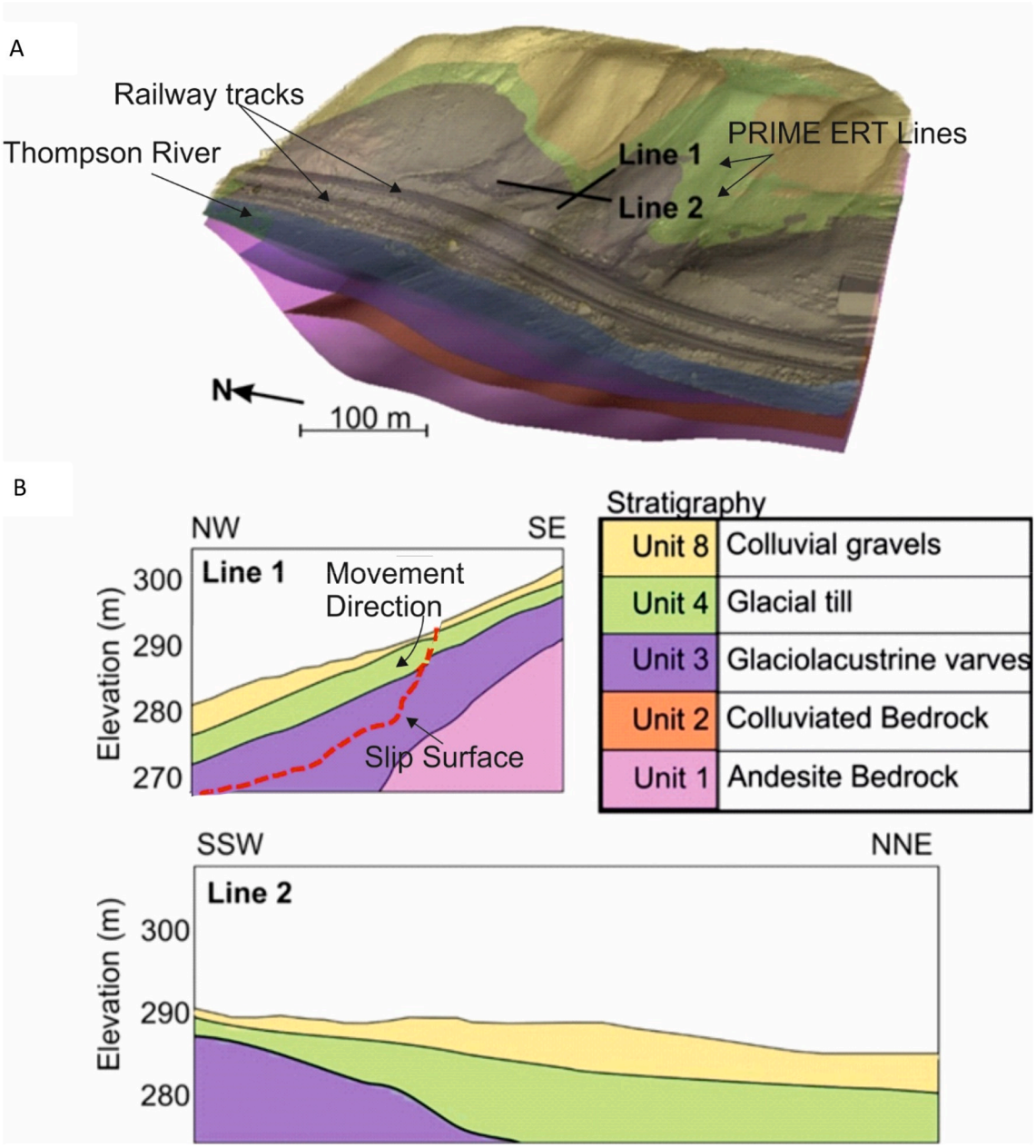

Fig. 3. Geological setting of Line 1 and Line 2 of the PRIME system, taken from a 3D ground model. A) The location of the PRIME-monitored section of the slope is shown within the wider context of the site. The topography is shown (brownish layer), along with layers corresponding to the geological cross-section, as indicated by the stratigraphy key. The location of the Thompson River is shown in pale blue. B) Cross-sections of Lines 1 and 2 are shown. The location of the slip surface of the Ripley Landslide is shown in the cross section of Line 1 (red dashed line). BGS©UKRI. (For interpretation of the references to colour in this figure legend, the reader is referred to the web version of this article.)

Related to moisture content, soil suction (negative pore water pressure) is also a key control on slope stability (Toll et al., 2011), affecting shear strength and effective stress (Fredlund et al., 1978; Springman et al., 2003; Lu et al., 2010). Pore water pressure (determined by the moisture content of the soil) is a key parameter in the Mohr-Coulomb failure criterion, which describes the balance of forces acting on a slope. Indeed, in unsaturated soils, matric suction can increase shear resistance to enable slopes to remain stable beyond the critical friction angle for failure (Brooks and Anderson, 1995). Furthermore, small changes in soil suction in response to changing moisture conditions can alter sub-surface moisture conditions sufficiently to induce slope failure (Fredlund et al., 1978; Zhang and Wang, 2018). Given that moisture content is a key control on electrical resistivity, ERT has the potential to estimate soil suction indirectly (Piegari and Di Maio, 2013).

Since resistivity can be used as a proxy for moisture content, and, by extension, for soil suction, development of petrophysical relationships for specific soils can be used to calibrate resistivity models, which allows moisture content and soil suction to be assessed more directly. Indeed, several previous studies have used ERT to study the effects of moisture conditions on slope stability, and to monitor changes in moisture content through space and time (Lehmann et al., 2013; Supper et al., 2014; Gance et al., 2016; Uhlemann et al., 2017).

This study extends previous work by developing and applying laboratory derived resistivity – moisture content – suction relationships to the field scale monitoring of an active landslide. Specifically, a novel methodology is developed for the generation of calibration curves for petrophysical relationships that aim to relate resistivity to moisture content and soil suction (negative pore water pressure) directly. These

relationships are applied to resistivity models generated from long-term monitoring of a natural landslide that affects transport infrastructure in British Columbia, Canada. The overarching objective of the study is to demonstrate utility of integrated geophysical-geotechnical modelling to illuminate the evolving patterns (in space and time) of moisture content and soil suction in a heterogeneous slope undergoing active failure.

2. Field site – the Ripley Landslide, British Columbia, Canada

The Ripley Landslide is a small, slow-moving (3–55 mm/year) (Bunce and Chadwick, 2012), translational landslide, and is one of 14 active landslides along a 10 km stretch of the Thompson River Valley (Fig. 1a and b). Situated on the Thomson River Valley, a major transportation corridor that connects Vancouver to the rest of Canada and the US, there is significant interest in monitoring the stability of the Ripley Landslide. Along much of the river, railway tracks run alongside both banks, but geological constraints mean that at the location of the Ripley Landslide, both railway tracks (Canadian Pacific and Canadian National Railway lines) run along the same side of the river. As such, failure of the slopes at this point could result in complete blockage of transport to and from Vancouver, with potential to negatively affect railway infrastructure, terrestrial and aquatic ecosystems, public safety, communities, local heritage, and the economy.

Since 2013, the Ripley Landslide has been used as a geophysical test site, with the aim of developing insights into the processes that result in slope failure at this site, and at other sites along the Thompson River Valley (Huntley and Bobrowsky, 2014; Macciotta et al., 2014; Huntley et al., 2017; Huntley et al., 2019; Holmes et al., 2020; Huntley et al., 2020). Several geophysical surveys were carried out, including Electrical Resistivity Tomography (ERT), Ground Penetrating Radar (GPR), Fixed Frequency Electromagnetic Induction (FEM), Seismic Refraction, Multichannel Analysis of Surface Waves (MASW), and Acoustic Bathymetry (Huntley et al., 2017; Huntley et al., 2019). These surveys were useful in improving the understanding of the subsurface structure of the slope and informed the development of a 3-D ground model of the site (Holmes et al., 2020), used to set monitoring data in the context of the wider field site.

In 2017, an ERT monitoring system (PRIME – Proactive Infrastructure Monitoring and Evaluation) was installed on the head scarp of the Ripley Landslide (Huntley et al., 2019; Holmes et al., 2020) to provide a more detailed insight into changing subsurface moisture conditions through time, with a long-term aim of identifying precursors to movement to aid in the prediction of slope failure.

2.1. Field site – geological setting

The geology of the Thompson River valley is predominantly composed of glacial deposits, underlain by a moderately high relief bedrock lithology (Huntley et al., 2017) (Fig. 2). The Pleistocene unit, in which the shear surface of the landslides in the Thompson River valley is situated, is a 45 m thick unit of laminated silt and clay glaciolacustrine sediments (Eshraghian et al., 2007). The presence of these high-plasticity glaciolacustrine clays is important for slope stability, given that most failures occur in this unit. This is explained by the internal friction angle of the clays, which range between 9° and 13° (Porter et al., 2002).

However, given that the landslides have been reactivated in the Thompson River valley following initial failure due to post-glacial incision into the Pleistocene valley fill by the Thompson River, the failures occur on pre-existing ruptures so the Mohr-Coulomb parameters that control slope stability are residual parameters (Eshraghian et al., 2007). The residual friction angle of clay soils is stress dependent, with higher normal stresses producing alignment of clay particles during shear, so resistance at the toe of a slope where normal stresses are lower is greater (Porter et al., 2002). As such, erosion of the toe of the Ripley Landslide by the Thompson River is problematic, as it reduces the stability of the most stable zone of the slope (Stark and Eid, 1994; Hendry et al., 2015).

A 3-D ground model was produced for the Ripley Landslide, building upon work described by Holmes et al. (2020). This meant that petrophysical relationships unique to each material type present in the monitored section of the slope could be applied to calibrate discrete sections of the ERT models produced from the PRIME monitoring.

GOCAD software (Mallet, 1992), used to digitize and visualize geological cross sections, borehole logs, and other subsurface data alongside digital elevation models (DEMs) and aerial photographs (Mallet, 1992), was used to produce a 3-D ground model of the Ripley Landslide field site, allowing for a greater understanding of how the geology of the site influences the processes affecting the slope stability (Fookes, 1997; Tye et al., 2011; Griffiths et al., 2012; Merritt et al., 2014; Thornton et al., 2018).

ERT images from previous surveys in 2013, which were carried out as part of a larger geophysical reconnaissance investigation of the landslide, were used as a baseline for the identification of lithological boundaries, along with borehole information and PRIME ERT data. Firstly, borehole logs, a DEM of the site, PRIME ERT models, and ERT models from reconnaissance surveys were imported into GOCAD. Previous geological interpretations (Huntley et al., 2017) were then used alongside this data to identify lithological boundaries, which were then digitized. These boundaries were then used to model surfaces, and finally to build the 3-D structure of the ground model. Geological cross-sections were then exported from GOCAD, for use in discretizing the ERT model mesh according to lithology. Geological cross-sections from the 3-D ground model are shown in Fig. 3.

As shown in Fig. 3, the monitored section of the Ripley Landslide is comprised of three dominant lithologies: Unit 3, Unit 4, and Unit 8. Unit 3, where the shear surface of the landslide is situated, is glaciolacustrine clay composed of finely laminated clay-silt couplets (varves) (Clague and Evans, 2003). Unit 4 is silt-rich lodgement till deposited during the Late Wisconsinan Fraser Glaciation (Clague and Evans, 2003; Eshraghian et al., 2007; Huntley and Bobrowsky, 2014). Unit 8 is interpreted as post-glacial colluvial material deposited by the Thompson River (Clague and Evans, 2003; Eshraghian et al., 2007).

The 3-D ground model produced here aids in the interpretation of hydrogeological changes through time through enabling lithology-specific calibrations for gravimetric moisture content and matric suction to be applied to corresponding zones of the ERT models.

3. Methodology

3.1. Electrical resistivity monitoring

In November 2017, two linear electrode arrays with a 2 m spacing between stainless steel pin electrodes were installed across the head scarp of the Ripley Landslide; one 53 m long with 27 electrodes, parallel to the steepest slope gradient, the other 91 m long with 45 electrodes in the perpendicular direction. A PRIME system was used to automatically generate measurement sets from the arrays every 12 h, with data transferred from site remotely via a telemetric link, enabling near-real time data processing and interpretation. The location of the PRIME monitoring arrays relative to the previous survey locations is shown in Fig. 1c. The data were measured using dipole-dipole configurations, with dipole lengths of 1–8 electrode spacings (short line) or 1–12 electrode spacings (long line) and dipole separations of 1–8 dipole lengths, to provide data with high image resolution (Crawford et al., 2018).

The data were processed as detailed in Holmes et al. (2020). In brief, data with contact resistances >10 kΩ were removed from the dataset, along with measurements with negative transfer resistances. Contact resistances of the electrodes were low in summer, with minimum, maximum, average and standard deviation (in brackets) values of 290, 1750, and 820 Ω (290 Ω) respectively. Winter contact resistances were higher owing to localized freezing at the surface of the slope, with

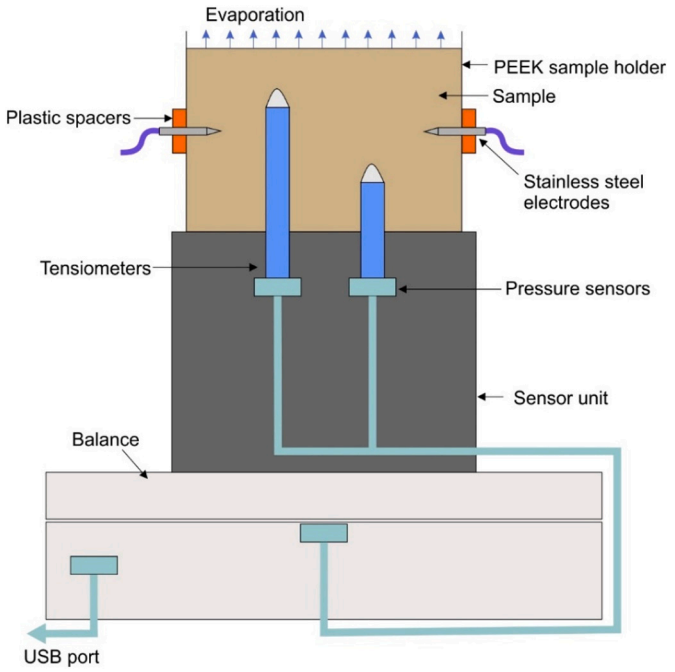

Fig. 4. Cross-sectional view of modified HYPROP experimental set-up. BGS©UKRI.

minimum, maximum, average and standard deviation of 1300, 14,000 and 6000 Ω (2400 Ω) respectively (Holmes et al., 2020). Measurements with large reciprocal errors (>5%) were also filtered out of the dataset. On average, up to May 2019, 7.47% of the data had reciprocal errors greater than 5%, and post-May 2019, this increased to an average of 44%. This may be indicative of a system issue, and investigations are ongoing. However, the remaining data still seem to be sufficient to produce reasonable models (Holmes et al., 2020).

Data were then inverted using an iteratively reweighted Gauss–Newton least-squares method (Res3DInvX64 from Geotomo Software) with an L1 norm on the data misfit, an L1 spatial smoothness constraint and an L2 temporal smoothness constraint. To correct for the influence of temperature, a simple temperature model was fitted to the data as a function of time and depth (Chambers et al., 2014), using data from temperature sensors in the air and at five different depths in the slide mass. It was assumed that this model was valid at all positions in the monitoring area and that the coupling coefficient was −2% per °C throughout the subsurface.

Holmes et al. (2020) presented initial observations from the first two years of monitoring from the PRIME system on the Ripley Landslide. The ERT models revealed complex hydrogeological pathways inferred from resistivity data, critical in determining moisture distribution within the slope. This work is built upon here, using laboratory-based petrophysical relationships to calibrate these models to provide insight into the changes in moisture content and soil suction through time, as opposed to using electrical resistivity as a qualitative proxy for these important factors in slope stability.

3.2. Development of petrophysical relationships – suction-resistivity and moisture content-resistivity experiments

For a particular soil type, both the resistivity (Waxman and Smits, 1968) and the soil suction (soil water characteristic curve) depend strongly on the moisture content. Therefore, it is possible to determine a quantitative relationship between soil suction and resistivity. These two parameters are typically measured independently of each other, however: suction measurements are made using point measurements from tensiometers, whereas larger volumes of the subsurface influence resistivity measurements (Piegari and Di Maio, 2013). Here, a new laboratory methodology for the simultaneous measurement of soil suction and electrical resistivity provides the opportunity to develop experimental relationships between resistivity, suction, and moisture content.

A modified HYPROP 2 system (METER Group) was used to develop petrophysical relationships for the main lithological units identified in the PRIME monitored section of the slope from the 3-D ground model. Undisturbed samples were taken of each lithological unit. The HYPROP 2 is designed for quick and easy development of soil moisture characteristic curves. Two tensiometers positioned at different heights within a drying sample measure the soil suction at each point (accurate to ±2.5 hPa) and a mass balance records the mass of the sample (accurate to ±0.01 g) for calculation of moisture content through time.

Modification of the HYPROP 2 equipment enabled resistivity to be measured at the same time as suction and moisture content. This is important as the same volume of material is used for each parameter measurement. The set-up of the modified HYPROP 2 is shown in Fig. 4. The original stainless-steel sample container was replaced with a non-conductive Polyether ether ketone (PEEK) container of the same dimensions (250 cm^3). Four equally-spaced electrodes (1 cm in length) were then inserted into the sample and connected to an ES-2 sensor (METER Group) which allowed electrical conductivity to be measured (accurate to ±10%) simultaneously with the suction and moisture content which the HYPROP 2 was originally designed to measure.

The suction-moisture content-resistivity experiments were carried out for Unit 3 and Unit 4, which comprise the majority of the monitored volume of the Ripley Landslide (Fig. 3). Unit 8 was not suitable for use in this experiment as it was too coarse-grained, making insertion of tensiometers and rod electrodes impossible without damaging the tensiometers. Unit 8 was also considered to have a less of an influence on slope stability than Unit 3 and 4, so testing was focussed on the more important units for slope stability (Sattler et al., 2021).

The petrophysical relationships developed in the laboratory were applied to discrete sections of the resistivity models, using the 3-D ground model to determine which relationship should be applied to each part of the model.

3.2.1. Resistivity-moisture content relationship

A relationship can be defined to allow electrical resistivity to be used as a direct indicator of soil moisture content.

The original Waxman-Smits model relates resistivity (ρ) to saturation (S):

$$\rho = \frac{F}{S^n}\left(\frac{1}{\rho_w} + \frac{B_{ws}Q_v}{S}\right)^{-1} \quad (1)$$

where, F is a formation factor, n is the saturation exponent, ρ_w is the pore water resistivity, B_{ws} is the average mobility of the cations, and Q_v is cation concentration per unit pore volume. However, the use of porosity is problematic here as due to shrink-swell behaviour, porosity varies with moisture content in materials with a high clay content (Chambers et al., 2014). As such, a modified Waxman-Smits model was fitted to the resistivity and moisture content data measured in the laboratory, as in Uhlemann et al. (2017):

$$\rho(GMC) = F\left(\frac{(1-\varphi)D_g GMC}{\varphi D_w}\right)^{-n}\left(\sigma_w + B_{ws}\left[\frac{(1-\varphi)D_g C}{100\varphi}\right]\left[\frac{\varphi D_w}{(1-\varphi)D_g GMC}\right]\right)^{-1} \quad (2)$$

Table 1
Parameters used in the fitting of Waxman-Smits models to laboratory data from the Ripley Landslide (Formation factor, *F*, a fitting parameter, *n*, porosity, *Φ*, grain density, D_g, water density, D_w, pore water conductivity, σ_w, average mobility of cations, B_{ws}, and cation exchange capacity, *C*).

Waxman-Smits model	F (–)	n (–)	Φ (%)	D_g (g/cm^3)	D_w (g/cm^3)	σ_w (S/m)	B_{ws} (S cm^3 m^{-1} meq^{-1})	C (meq/100 g)
Unit 3 High GMC (>0.26 GMC)	35.576	3.481	37.2	2.53	1	0.0330	1.91	17.4
Unit 3 Low GMC (<0.12 GMC)	25.364	2.272	37.2	2.53	1	0.0330	1.91	17.4
Unit 4 High GMC (>0.34 GMC)	22.224	2.333	48.0	2.53	1	0.0528	1.95	17
Unit 4 Low GMC (<0.043 GMC)	19.600	3.256	35.0	2.53	1	0.0528	1.95	17

where, φ is porosity, D_g is grain density (g cm^{-3}), D_w is water density (g cm^{-3}), σ_w is the pore water conductivity (S/ m), and *C* is cation exchange capacity (meq/100 g). The average cation mobility, B_{ws} (S cm^3 m^{-1} meq^{-1}), was estimated from the empirical fit given by Waxman and Smits (1968). Each parameter was measured in the laboratory, with the exception of *F* and *n*, which were fitted (there is uncertainty in these values as although these values fit the data, they are not unique) and *Bws*, which was estimated (Waxman and Smits, 1968):

$$B_{ws} = 4.6\left(1 - 0.06\,Exp\left[-\frac{\sigma_w}{1.3}\right]\right) \quad (3)$$

Waxman-Smits models were fitted to the data from each lithological unit tested in the laboratory (Unit 3 and Unit 4, which are the most important lithological units in terms of slope movement (Sattler et al., 2021)) in order to convert electrical resistivity to gravimetric moisture content.

3.2.2. Resistivity-suction relationship

A relationship between soil suction and electrical resistivity can be established. Modified from Fredlund and Xing (1994), Eq. (4) relates gravimetric moisture content (GMC) with soil suction (ψ):

$$GMC = GMC_s\left[\frac{1}{ln\left[e + (\psi/a)^t\right]}\right]^b \quad (4)$$

where GMC_s is gravimetric moisture content at saturation (g g^{-1}), *e* is Euler's number, and *a*, *t*, and *b* are fitting parameters.

This model was fitted to the laboratory-measured data for Unit 3 and Unit 4 to describe the relationship between moisture content and soil suction. These relationships were then used in conjunction with the resistivity-moisture content relationships to develop a relationship between resistivity and soil suction, as expressed by: $\rho(\psi) = \rho(GMC(\psi))$.

3.3. Field sensor measurements

Two boreholes instrumented with TEROS-21 soil suction sensors were installed in November 2017 at the head scarp of the landslide (Fig. 1c), covering a range of depths from 0 to 2 m below the surface. The sensors were installed in Unit 8 (Fig. 3). TEROS-21 sensors measure water potential, which is the potential energy of the water in equilibrium with water in the soil. The measurement of water potential here is based on the Second Law of Thermodynamics, whereby connected systems with differing energy levels move toward an equilibrium energy level. As such the water potential of the sensor comes into equilibrium with that of the soil. These sensors gathered matric suction data for the entirety of the 2-year monitoring period at the Ripley Landslide to an accuracy of ±10% of the reading.

Effective rainfall – total rainfall minus evapotranspiration – was also calculated, using the rainfall data from a rain gauge installed at the site. Here, evapotranspiration was calculated using the Hargreaves-Samani equation (Hargreaves and Samani, 1982; Samani, 2000), which uses temperature (measured on site), and latitude to estimate evapotranspiration:

$$ET = 0.0135(KT)(R_a)(TD)^{1/2}(TC + 17.8) \quad (5)$$

where *ET* is evapotranspiration, *KT* is an empirical coefficient, *TD* is temperature difference between the maximum and minimum recorded temperature (°C) ($T_{max} - T_{min}$), and *TC* is the average daily air temperature (°C).

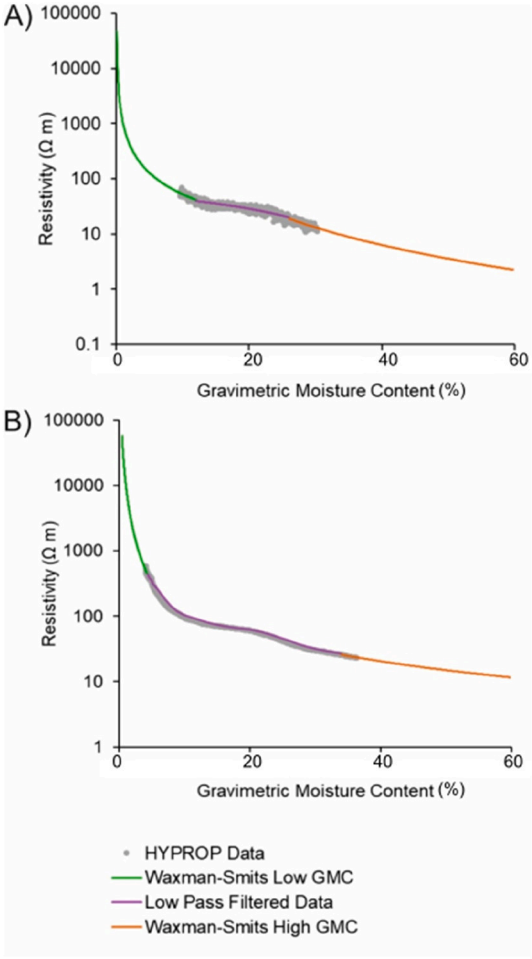

Fig. 5. Moisture content-resistivity relationships for Units 3 (A) and 4 (B), both measured in the laboratory using the modified HYPROP 2, fitted with Waxman-Smits models, and with low-pass filters in the region of the inflection in the curves. BGS©UKRI.

3.4. Ground movement data

Interferometric Synthetic Aperture Radar (InSAR) data was used to measure ground movement associated with the Ripley Landslide over the study period. InSAR has been used for monitoring landslide movement as surface deformation results in a phase shift of the backscattered microwave signal between acquisitions, so that surface movement can be identified with high spatial resolution (Carlà et al., 2019). Here, Sentinel-1 data from the European Space Agency, which provides high-precision (mm-cm) measurements at medium spatial resolution where signal is good (Wasowski and Bovenga, 2022) was used to determine the

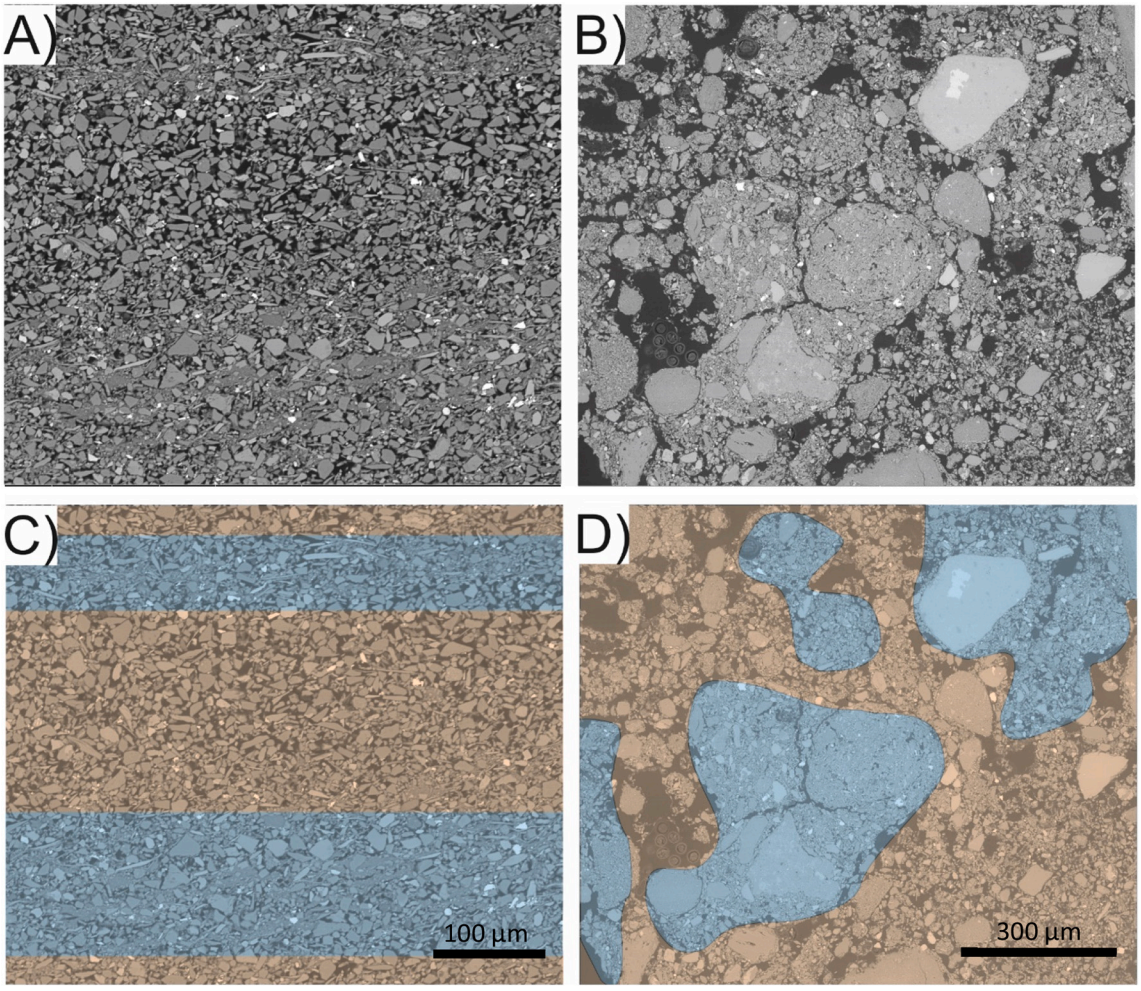

Fig. 6. Images of the material fabric at the Ripley Landslide, from Unit 3 (A), and Unit 4 (B). Images were taken of a thin section of each material viewed under a Scanning Electron microscope (SEM). Images (C) and (D) show the same images from Unit 3 and Unit 4, respectively, coloured to show regions of finer-grained material and lower porosity (blue), and regions of coarse-grained material and higher porosity (orange). BGS©UKRI. (For interpretation of the references to colour in this figure legend, the reader is referred to the web version of this article.)

rate of displacement due to landslide activity (data from Huntley et al., 2021). The PRIME-monitored section of the slope was selected (91 m × 54 m), and the displacement of 45 points within this zone, was monitored through time.

4. Results and discussion

4.1. Petrophysical relationships

4.1.1. Resistivity-moisture content relationship

Owing to the material fabric of the lithological units tested in the laboratory, there is an inflection in the resistivity-moisture content curve, so Waxman-Smits curves were fitted independently to the data outside the inflection region for each of the units, and the inflection region is modelled with a low pass filter of the data. Parameters used for the fitting of the Waxman-Smits models are shown in Table 1. The modelled relationships are shown in Fig. 5. The inflections are attributed to the presence of different scales of porosity within the samples. SEM images of each lithological unit are shown in Fig. 6. Clear laminations are seen in Unit 3, with layers of coarser grains and larger pore spaces and layers of finer grains with smaller pore spaces. Unit 4 does not exhibit this laminated structure, but areas of finer grains and smaller pore spaces within a more open matrix of coarser grains and larger pore spaces are observed.

At high moisture contents and associated low values of matric suction, we propose that there is a high level of electrical connectivity between pores across the whole sample. Fully connected fluid pathways within the sample contribute to the increase in electrical conductivity (or decrease in electrical resistivity) at high moisture contents. Indeed, in a study of hydraulic characteristics of soils at different bulk densities, and with different pore scales, Cimpoiasu et al. (2020) found that in near-saturated samples, the macroporosity alone dominated the measured electrical resistivity. As the sample dries and moisture content decreases during the course of the experiment, matric suction increases. The matric suction is higher in the fine-grained areas of the sample, which draws in moisture, thereby reducing the electrical connectivity of the fluid pathway across larger pores in the coarser-grained matrix of the material, resulting in an inflection in the moisture content-resistivity relationship. Therefore, it is suggested that at different moisture contents, different regions of the soil fabric dominate the relationship between moisture content and electrical resistivity, resulting in the need for multiple Waxman-Smits relationships for the calibration of electrical resistivity models within a single lithological unit.

When fitting the Waxman-Smits models to the data (as shown in Table 1), the value for the formation factor (F), depends strongly on the value of porosity. The true value of F cannot be identified from the fit of the Waxman-Smits model as it is non-unique; different values of porosity result in different values of F where the misfit and n remain constant.

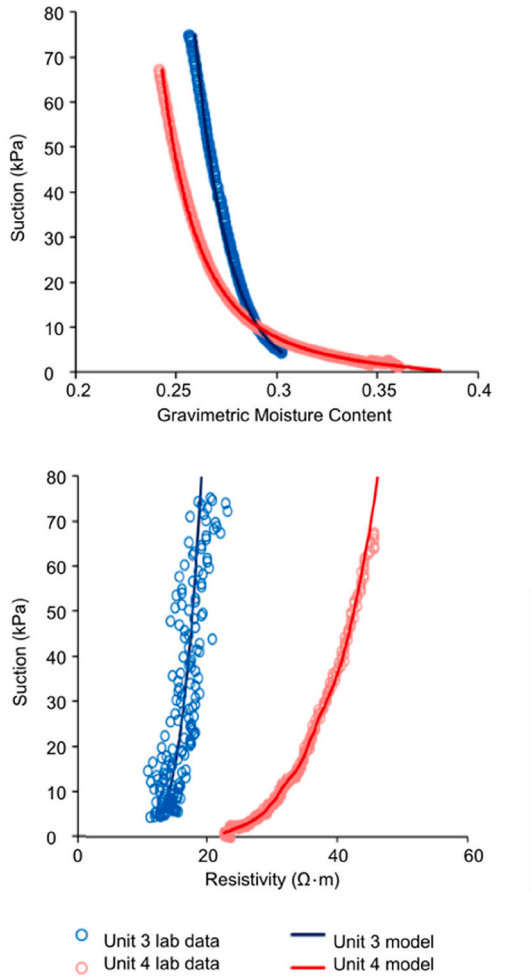

Fig. 7. Suction-moisture content relationships and resistivity-suction relationships for Units 3 and 4, both measured in the laboratory using the modified HYPROP 2. BGS©UKRI.

Table 2
Parameters used in the fitting of Suction-moisture content models to laboratory data from the Ripley Landslide. These parameters fit the data but are not unique, which is a limitation of the research as there is uncertainty in these values.

Suction-GMC model	GMC_S (%)	b (−)	a (−)	t (−)
Unit 3	37.2	0.761	44.70	0.290
Unit 4	39.1	0.305	13.90	1.221

Indeed, here, at low GMC for Unit 4, the same fit to the data can be achieved with a Formation Factor that is lower than that reported in Table 1 (3.396) if a higher porosity is used (0.48), along with the same value for n as reported in Table 1. However, the values reported in Table 1 are closer to those reported in other studies of fine-grained materials (e.g. Merritt et al., 2014, where, for a silty clay similar to that of Unit 4 in this study, $F = 22.17$, and porosity = 0.34). Further, it is expected that the porosity in the fine-grained region of the sample (which dominates the GMC-resistivity relationship at low moisture contents – as discussed above and highlighted in Fig. 6) will be lower than for the sample as a whole. As such, it is proposed that more reasonable values for the Formation Factor and porosity in the Low GMC section of the curve for Unit 4 are those reported in Table 1, as they are representative of fine-grained materials. While these values have considerable uncertainty, the resulting Waxman-Smits model is numerically identical and so these uncertainties do not affect the results that depend on the fit.

4.1.2. Resistivity-suction relationship

The relationships between soil suction and GMC (Soil moisture characteristic curve) and between soil suction and resistivity for units 3 and 4 of the Ripley Landslide is shown in Fig. 7, with the modelled relationship shown alongside the laboratory-measured data. The values of the parameters used to fit the relationship between suction and GMC are shown in Table 2. These relationships were applied to the ERT models produced from the field monitoring to provide an insight into the changes in soil suction through time, as discussed below.

4.2. Landslide movement

Fig. 8 shows the cumulative ground displacement below the head scarp of the Ripley Landslide, within the area of the PRIME monitored section of the slope (Huntley et al., 2021). There was an average of 9 cm of displacement over two years, with the greatest rate of movement occurring over winter between October and April. This movement occurred uniformly across the slope, except for one point, so the effect of the slope movement on electrode movement and the resulting ERT inversions presented here is likely to be minimal (Wilkinson et al., 2010; Wilkinson et al., 2016). The period of accelerated movement in winter coincides with the freeze-thaw cycling that the Ripley Landslide undergoes each year when air temperature drops below 0 °C. The slope stabilizes during the spring and summer months, when moisture content in the Ripley Landslide subsurface is at its highest. Movement increases as resistivity increases toward the point of freezing during the winter months. The period of increased movement also coincides with low river levels of the Thompson River at the toe of the Ripley Landslide. River levels fluctuate by up to 7 m annually (Sattler et al., 2021), and when the River level is low, this leads to a de-buttressing effect (Eshraghian et al., 2007) and accelerates movement up until the point of snowmelt in April when river levels increase again.

4.3. Calibrated resistivity models

Moisture content - resistivity relationships developed in the laboratory were applied to the ERT models from the PRIME monitoring. A baseline image of spatial distribution of gravimetric moisture content (GMC) from the beginning of the monitoring period on 05/12/2017 is shown in Fig. 9a. Fig. 9b shows the model divided into zones based on the 3-D ground model of the site. Petrophysical relationships were applied to the zones of the model constituted by Unit 3 and Unit 4. Areas of the model for which no GMC data is available are shown. Zones of the model which were not calibrated are displayed as a gravimetric moisture content value of 0.

Changes in gravimetric moisture content through time, as a percentage change from a baseline moisture content condition from December 2017, are shown in Fig. 9c. The constraints used in the data inversion were found to produce convincing results with regard to the changes in resistivity through time in response to changing weather conditions in the top few metres of the model. However, where the model resolution is low (e.g. at depth) it is possible that the L2 temporal constraint could be causing the changes to overshoot, producing possibly spurious changes in resistivity (Holmes et al., 2020), and therefore in the calibrated GMC, at depth. As such, interpretations of changes in GMC focus on the upper few meters of the model. Additionally, although these models are corrected for seasonal temperature changes (Uhlemann et al., 2017), rapid near-surface changes in temperature will affect the translation of resistivity to moisture content. It is also assumed here that changes in porosity are minimal, and that the resistivity of the water in the slope is also consistent. Each of these factors is important in the fitting of the Waxman-Smits models, and so this is a potential limitation of the research.

There is a clear seasonal pattern of ground moisture conditions at the

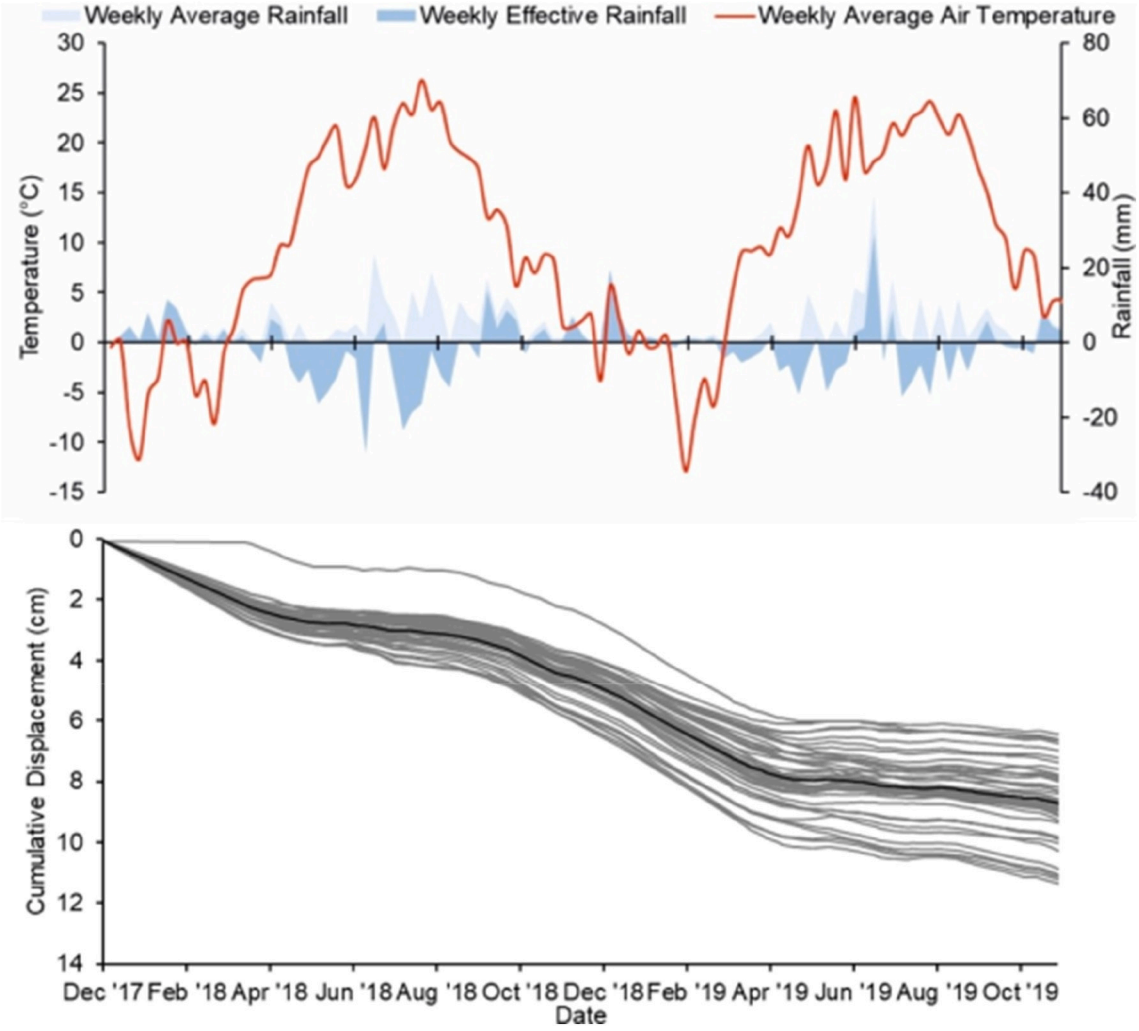

Fig. 8. Cumulative displacement of points on the Ripley Landslide (grey) and average cumulative displacement (black), shown alongside meteorological data for the same period. Weekly average temperature is shown, along with weekly average rainfall and weekly effective rainfall. BGS©UKRI, contains ©Geological Survey of Canada data.

Ripley Landslide. The greatest changes in GMC are seen in the spring at the onset of the snowmelt season (Fig. 9c). The propagation of the wetting front down the slip face is apparent; an increase in gravimetric moisture content in this zone is observed directly following the onset of the snowmelt period each year (March–April), as well as in response to positive weekly effective rainfall, particularly in the very near-surface. The GMC of the slip face zone remains elevated following the propagation of the wetting front for several months, with implications for slope stability as high moisture contents are associated with a decrease in normal effective stress, therefore increasing susceptibility to failure.

The influence of temperature on changes in electrical resistivity and calibrated GMC is important at the Ripley Landslide as temperatures fall below 0 °C on a seasonal basis (Fig. 10a). However, the snow cover varied considerably over the monitoring period (Fig. 11), which influenced the mechanism for change in GMC at the onset of the snowmelt period. In 2018, there was a far greater snow cover than in 2019. Snow has insulating properties, and so the subsurface temperature remained elevated in 2018 compared with 2019 reducing the depth of freezing, and in the head scarp zone where snow drift accumulates, temperatures remained above 0 °C throughout the entire monitoring period. Therefore, the increase in gravimetric moisture content seen in Fig. 10b and c at the onset of the snowmelt season in 2018 is likely to be due to infiltration of snowmelt combined with melting of ice in the subsurface, whereas in 2019, this is likely to be associated solely with melting of ice in the subsurface.

Fig. 10b shows the changes in GMC alongside air temperature and weekly effective rainfall. GMC was isolated on the calibrated PRIME model for the head scarp zone and the non-head scarp zone, as delineated by the regions of low resistivity in the head scarp zone and higher resistivity in the non-head scarp zone and the average GMC of the cells in each zone was calculated. As air temperature rises above 0 °C in the spring, there is a rapid increase in GMC in the head scarp zone as the snowmelt season begins. GMC rises throughout the spring, peaking in summer, and then falling again to a minimum in winter. This is likely to be due to freezing in the near surface. As shown in Fig. 10c, the moisture content of the head scarp zone remains elevated compared with that of the rest of the PRIME-monitored area of the slope all year round. This is likely to cause a reduction in matric suction and normal effective stress in this zone, increasing the likelihood of failure. Changes in the absolute values of GMC in the head scarp zone are also far greater, ranging from a minimum of 35% to a maximum of 49%, compared with 10% to 16% across the rest of the slope. There is also a lag of approximately 2 weeks between the changes in air temperature and the subsurface changes in GMC.

In terms of percentage change though, the magnitude of change is similar (Fig. 10b). However, the head scarp zone responds more quickly to both wetting and drying in response to snowmelt and to changes in effective rainfall than the rest of the slope does, as shown by the

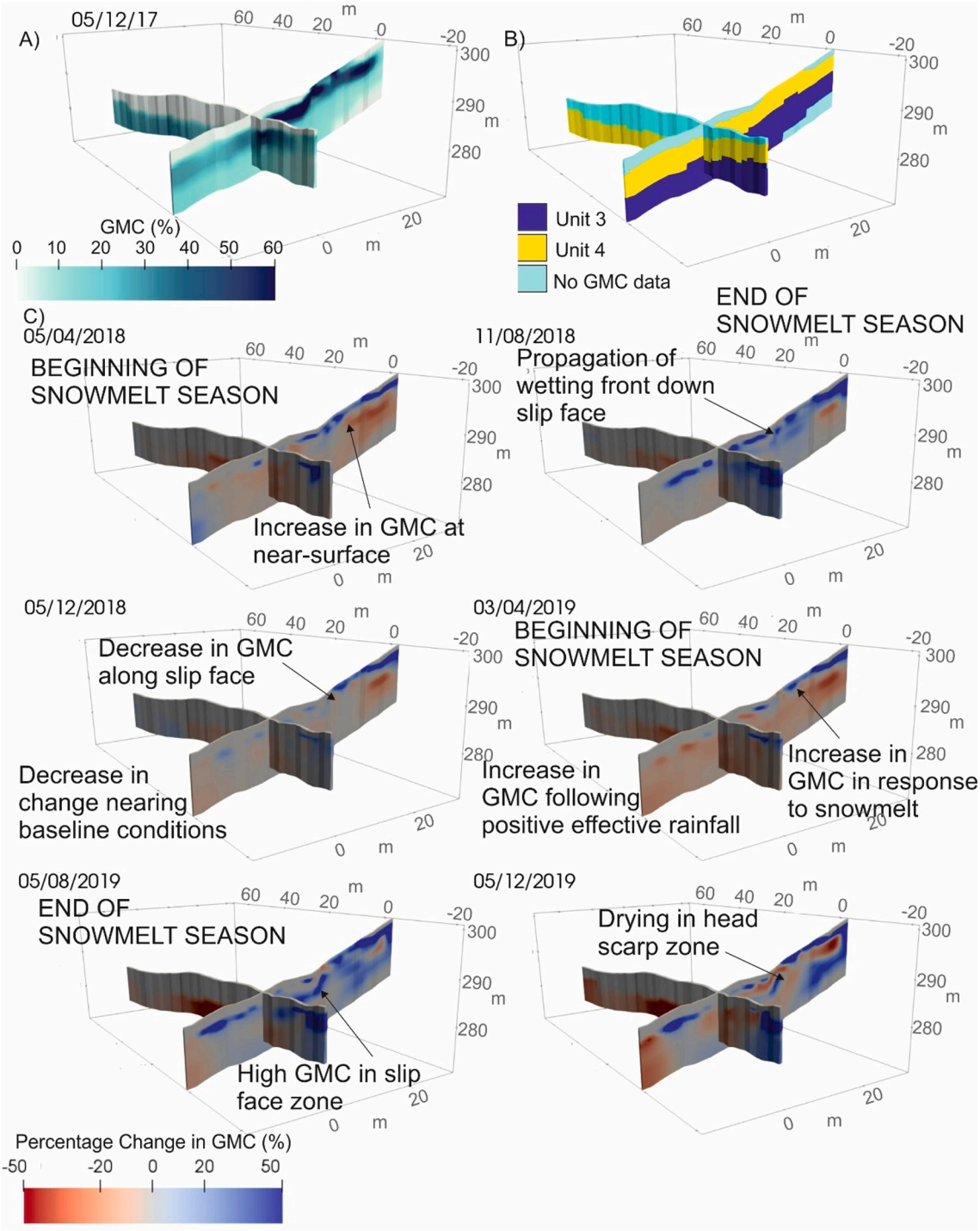

Fig. 9. A) Baseline Image from the Ripley Landslide ERT monitoring (05/12/17), calibrated using laboratory-based petrophysical relationships to display gravimetric moisture content (GMC). B) Regions of the model calibrated by petrophysical relationships from Unit 3 and Unit 4, and regions of the model for which there is no GMC data available. C) Percentage change in gravimetric moisture content (GMC) from baseline image (05/12/17) through two years of monitoring. BGS©UKRI.

steepness of the rising and falling limb. Indeed, during the 2018 snowmelt period (March to May), there was an average rate of increase in GMC of 0.9% per week in the head scarp zone compared with 0.3% per week in the rest of the slope (Fig. 9). This is likely to be due to the presence of tension cracks in the head scarp zone, which provide a preferential pathway for moisture movement. Additionally, the percentage decrease in GMC in winter was lower in the head scarp zone than in the rest of the slope. This is likely to be due to the exaggerated effects of freezing across the slope compared with the head scarp, as more snow tends to accumulate in the sheltered head scarp zone (Fig. 11). There is little response to changes in effective rainfall in the subsurface, with the exception of in the head scarp zone. This is due to the depth of the zone of study here, as changes in electrical resistivity in the very near surface occur predominantly in Unit 8 (Holmes et al., 2020), for which no GMC data is available. Therefore, changes in GMC presented here are seasonal, rather than changing rapidly in response to surface forcing factors such as rainfall events.

There is a clear relationship between electrical resistivity and matric

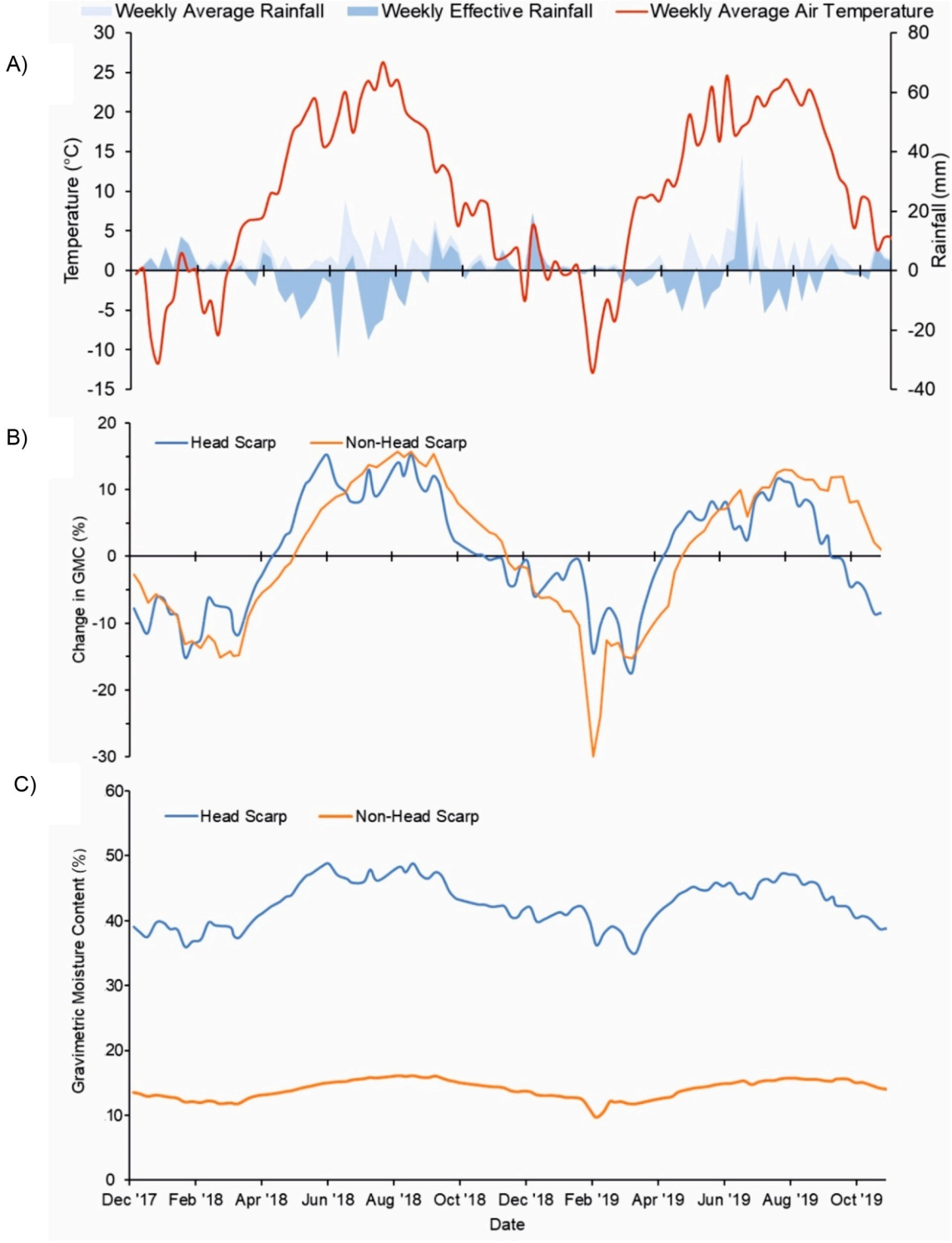

Fig. 10. A) Weekly average temperature, weekly rainfall, and weekly effective rainfall through time. B) Percentage change of the average gravimetric moisture content for the top 5 m of the ERT model (excluding non-calibrated zones), showing the head scarp and non-head scarp change separately. C) Absolute values of gravimetric moisture content through time for head scarp and non-head scarp regions of the upper 5 m of the PRIME monitored areas of the landslide based on laboratory calibrations of ERT models. BGS©UKRI.

suction in the Ripley Landslide materials (Fig. 7). This relationship was used to calibrate ERT images from the Ripley landslide, and average suction in Unit 4, where the failure surface of the Ripley Landslide lies, was calculated. Changes in the modelled soil suction through time are shown in Fig. 12. Field measurements of soil suction are shown alongside this: In both the measured and modelled data, there are higher suctions in winter and lower suctions in spring following the onset of the snowmelt season. It should be noted that the modelled suctions based on the calibrated resistivity models shown here (Fig. 12) are well beyond the range of suctions measured in the laboratory (Fig. 7). However, the suctions measured in the field and the modelled suctions have a moderate Pearson correlation coefficient of 0.40. Although not strong, this

Fig. 11. Photographs taken by wildlife cameras installed along the PRIME lines at the Ripley Landslide: (A) A snapshot from the time of maximum snow coverage in 2018 (02/01/2018), and (B) the maximum snow coverage in 2019 (14/02/2019) is shown. Most snow accumulation is observed in the head scarp zone (A).

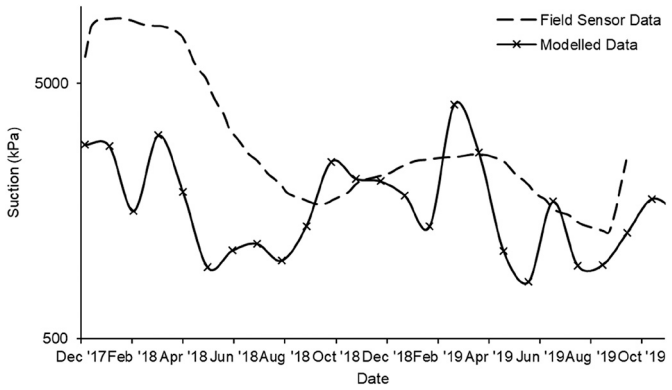

Fig. 12. Changes in soil suction through time in the Ripley Landslide, showing modelled data from calibrated ERT models, and field sensor data. BGS©UKRI.

correlation is present despite the fact that the field measurements of soil suction were taken in a different unit (Unit 8), for which no calibration was available. Further, measurements were taken for a discrete point on the slope (Fig. 1c), whereas the modelled suction is based on an average for a greater volume of the slope.

Additionally, changes in soil suction through time, as recorded by the suction sensors installed on the site at the Ripley Landslide, are shown in Fig. 13. Changes in resistivity recorded by the PRIME system in the cells of the ERT mesh in the location of the suction sensors are shown alongside this, enabling an indirect comparison. These changes follow a similar trend with higher suctions corresponding to higher values of resistivity. Changes in suction mirror changes in moisture content (Fig. 9), as there is a monotonic relationship between moisture content and soil suction. The extremely high suctions recorded in the summer of 2018 (maximum = 26,592 kPa) are likely to be due to high rates of evapotranspiration due to high air temperatures and increased plant activity during the summer months. Indeed, the summer of 2018 was drier than that of 2019 (Sattler et al., 2021), explaining the higher levels of suction in 2018 compared to 2019. Again, the rapid change in winter, whereby soil suction increased sharply, is likely to be due to freezing in the near surface and a reduction in the quantity of liquid water in the subsurface, given the role of temperature in controlling changes in electrical resistivity at the Ripley Landslide (Sattler et al., 2021).

This has important implications for slope stability as snowmelt occurs earlier in the Thompson River Valley than at higher elevations (Sattler et al., 2021). As such, when matric suction in the Ripley Landslide begins to fall in spring (Fig. 13), river levels remain low prior to increasing in spring in response to snowmelt in the wider catchment. Therefore, the Ripley Landslide is vulnerable to slope failure at this point as matric suction is low at the same time as the river buttressing effect is at a minimum (Sattler et al., 2021). As such, while moisture content variations are important for slope stability in the upper reaches of the slope, there are also other controlling factors that need to be considered in slope stability assessment.

4.4. *Temperature-resistivity-suction relationships*

The relationship between soil suction, resistivity, and temperature is considered in Fig. 14. Here, temperature measured by TEROS-21 soil

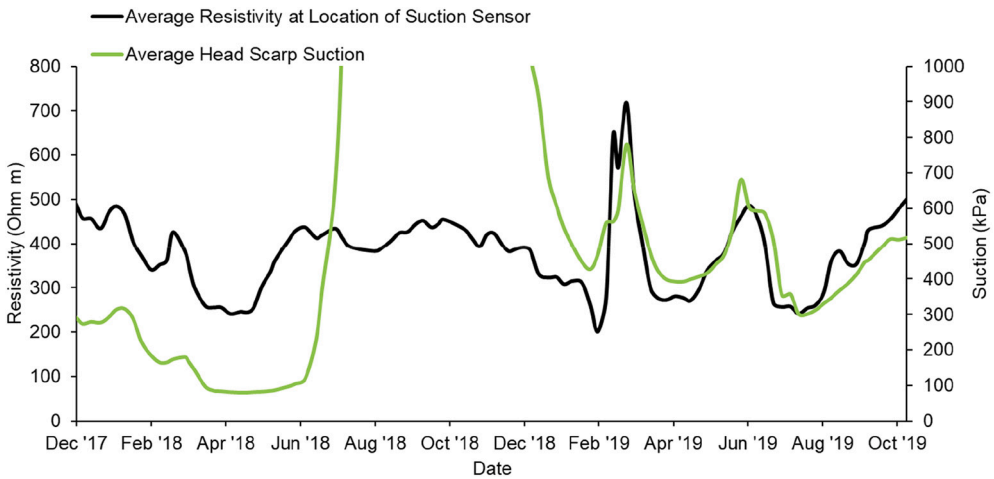

Fig. 13. Changes in soil suction, as measured by the TEROS-21 sensors, and co-located electrical resistivity through time in the Ripley Landslide. Data courtesy of the University of Saskatchewan. BGS©UKRI.

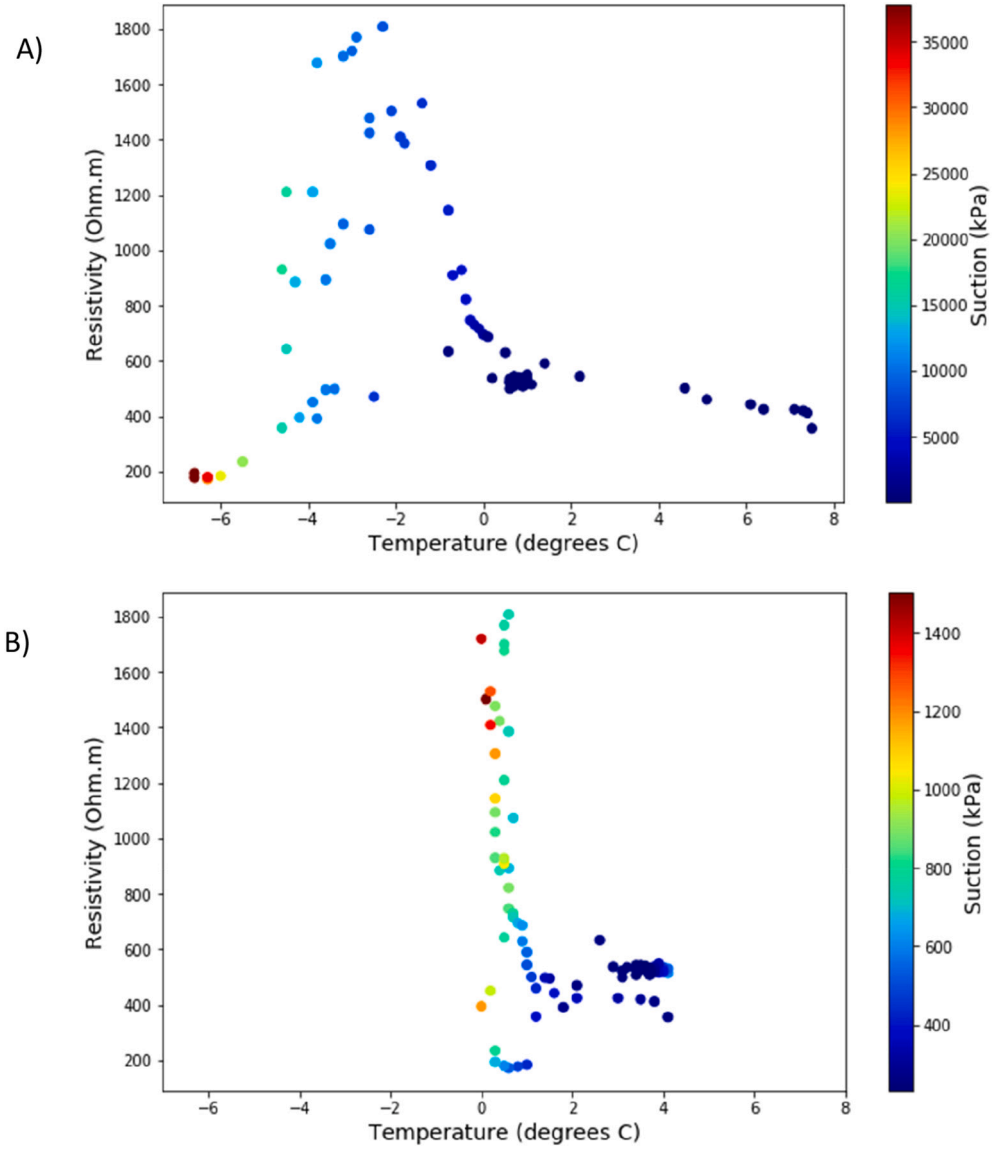

Fig. 14. Field-based relationship between resistivity and temperature, coloured according to matric suction, for different zones of the Ripley Landslide: A) Slide mass relationships, B) Head scarp relationships. BGS©UKRI.

suction sensors installed on the Ripley Landslide is plotted against the average temperature-corrected resistivity of the ERT images in the vicinity of the sensors. In the head scarp zone, suction and resistivity rise in line with decreasing temperatures, as expected (Wu et al., 2013). In the slide mass zone, however, whilst resistivity increases with decreasing temperatures above 0 °C, temperatures fall below 0 °C in this area as typically less snow covers this area and so there is less insulation, and so freezing occurs.

The low resistivity values at very low temperatures are attributed to the supercooling effect, which is characterised by drops in resistivity, followed by sharp increases (Krautblatter et al., 2010; Wu et al., 2013). As shown in the time-series resistivity data (Fig. 13), there is a period of low resistivity at the onset of freezing, while suction values begin to rise and temperatures fall. This initial low resistivity at the onset of freezing can be attributed to an increase in the salinity of the unfrozen pore fluid as ice begins to nucleate which results in separation of salts from the pore fluid. This results in a high salt concentration in the frozen zone, increasing the conductivity of the pore solution and decreasing soil bulk resistivity. It follows that a high concentration of salts at the boundary of the freezing front results in salt migration into the unfrozen zone (Bing et al., 2015). Hence, the resistivity of the near surface begins to increase following this initial drop in resistivity, and peaks as the ground becomes fully frozen at the near surface (Figs. 13 and 14). As such, where temperatures fall below 0 °C, the relationships between resistivity, soil suction, and temperature become more complex, as additional processes should be considered.

5. Conclusions

The 4-D ERT monitoring presented here allows an assessment of the long-term behaviour of a slope affecting transport infrastructure: Complex hydrogeological pathways are highlighted within the PRIME-monitored section of the Ripley Landslide. Petrophysical relationships developed in the laboratory allow ERT to be used to provide insight into moisture content and soil suction changes through time in response to changing weather conditions, which furthers the understanding of slope behaviour at this site. Here, snow melt events are the main driver of moisture content changes in the subsurface, as freeze-thaw cycles result in significant spring-time changes in infiltration as a result of snowmelt. This coincides with an annual period of accelerated movement of the landslide from October to April, attributed to a de-buttressing effect at the toe of the Ripley Landslide owing to low levels of the Thompson

River during this time. Freeze-thaw processes have a unique signature on the resistivity of the subsurface, as shown in this study. Further consideration of the complex suction-resistivity relationships at the timing of freeze-thaw events during periods where temperatures fall below 0 °C provides an opportunity for further research in the future. This study demonstrates the utility of geoelectrical monitoring for assessing slope stability in moisture-driven landslides, highlighting subsurface changes that cannot be inferred from traditional transport infrastructure monitoring techniques.

CRediT authorship contribution statement

Jessica Holmes: Conceptualization, Methodology, Investigation, Writing – original draft, Writing – review & editing, Visualization, Formal analysis. **Jonathan Chambers:** Conceptualization, Supervision, Methodology, Writing – review & editing. **Paul Wilkinson:** Conceptualization, Supervision, Software, Formal analysis, Writing – review & editing. **Philip Meldrum:** Methodology, Software. **Mihai Cimpoiaşu:** Formal analysis, Writing – review & editing. **James Boyd:** Investigation. **David Huntley:** Resources, Supervision. **Paul Williamson:** Software. **David Gunn:** Methodology. **Ben Dashwood:** Methodology. **Jim Whiteley:** Conceptualization, Writing – review & editing. **Arnaud Watlet:** Conceptualization, Software. **Matthew Kirkham:** Resources. **Kelvin Sattler:** Resources. **David Elwood:** Resources. **Vinayagamoothy Sivakumar:** Supervision. **Shane Donohue:** Conceptualization, Supervision, Methodology, Writing – review & editing.

Declaration of Competing Interest

The authors declare that they have no known competing financial interests or personal relationships that could have appeared to influence the work reported in this paper.

Acknowledgments

This research is a collaborative effort from government agencies (the Geological Survey of Canada, and the British Geological Survey), Railway industry partners (Canadian National Railway, and Canadian Pacific Railway), and universities (Queen's University Belfast, and University College Dublin). BGS authors publish with permission of the Executive Director of the BGS (UKRI). The first author was funded by the Department for the Economy, Northern Ireland and the British Geological Survey, and fieldwork was partially funded by the Victor Milligan Travel Scholarship (Queen's University Belfast). The BGS contribution is linked to the ACHILLES project (grant reference EP/R034575/1). The last author's contribution is funded with the financial support of Science Foundation Ireland, Geological Survey of Ireland and the Environmental Protection Agency under the SFI Frontiers for the Future Programme 19/FFP/6535".

References

Abdu, H., Robinson, D.A., Seyfried, M., Jones, S.B., 2008. Geophysical imaging of watershed subsurface patterns and prediction of soil texture and water holding capacity. Water Resour. Res. 44, W00D18.

Archie, G.E., 1942. The electrical resistivity log as an aid in determining some reservoir characteristics. Petrol. Trans. AIME. 146, 54–62.

Bing, H., He, P., Zhang, Y., 2015. Cyclic freeze-thaw as a mechanism for water and salt migration in soil. Environ. Earth Sci. 74, 675–681.

Brooks, S.M., Anderson, M.G., 1995. The determination of suction-controlled slope stability in humid temperate environments. Geografiska Ann. Ser. A Phys. Geogr. 77 (1/2), 11.22.

Bunce, C., Chadwick, I., 2012. GPS monitoring of a landslide for railways. In: Eberhardt, et al. (Eds.), Landslides and Engineered Slopes: Protecting Society through Improved Understanding, pp. 1373–1379.

Caine, N., 1980. The rainfall intensity: duration control of shallow landslides and debris flows. Geografiska Ann. Ser. A Phys. Geogr. 62 (1/2), 23–27.

Carlà, T., Intrieri, E., Raspini, F., et al., 2019. Perspectives on the prediction of catastrophic slope failures from satellite InSAR. Sci. Rep. 9, 14137. https://doi.org/10.1038/s41598-019-50792-y.

Chambers, J.E., Gunn, D.A., Wilkinson, P.B., Meldrum, P.I., Haslam, E., Holyoake, S., Kirkham, M., Juras, O., Merritt, A., Wragg, J., 2014. 4D electrical resistivity tomography monitoring of soil moisture dynamics in an operational railway embankment. Near Surf. Geophys. 12, 61–72.

Cimpoiasu, M.O., Kuras, O., Pridmore, T., Mooney, S., 2020. Hydrodynamic characterization of soil compaction using integrated electrical resistivity and X-ray computed tomography. Vadose Zone J. Spec. Sect. Agrogeophys. Geophys. Investig. Soil–Plant–Atmosph. Interact. Supp. Agric. Manag. 15. https://doi.org/10.1002/vzj2.20109.

Clague, J.J., Evans, S.G., 2003. Geological framework of large historic landslides in Thompson River Valley, British Columbia. Environ. Eng. Geosci. 9, 201–212.

Crawford, M.M., Bryson, L.S., Woolery, E.W., Wang, Z., 2018. Using 2-D electrical resistivity imaging for joint geophysical and geotechnical characterization of shallow landslides. J. Appl. Geophys. 157, 37–46.

Dijkstra, T., Dixon, N., Crosby, C., Frost, M., Gunn, D., Fleming, P., Wilks, J., 2014. Forecasting infrastructure resilience to climate change. Proc. Inst. Civ. Eng. 167 (TR5), 269–280.

Eshraghian, A., Martin, C.D., Cruden, D.M., 2007. Complex earth slides in the Thompson River Valley, Ashcroft, British Columbia. Geol. Soc. Am. 13 (2), 161–181.

Fookes, P.G., 1997. Geology for engineers: the geological model, prediction and performance. Q. J. Eng. Geol. 30, 293–424.

Francesco, P., Pandolfo, C., Stelluti, M., Berni, N., Brocca, L., Moramarco, T., 2012. Assessment of rainfall thresholds and soil moisture modelling for operational hydrogeological risk prevention in the Umbria region (Central Italy). Landslides. 9, 229–237.

Fredlund, D.G., Xing, A., 1994. Equations for the soil-water characteristic curve. Can. Geotech. J. 31, 521–532.

Fredlund, D.G., Morgenstern, N.R., Widger, R.A., 1978. The shear strength of unsaturated soil. Can. Geotech. J. 15, 313–321.

Gance, J., Malet, J.-P., Supper, R., Sailhac, P., Ottowitz, D., Jochum, B., 2016. Permanent electrical resistivity measurements for monitoring water circulation in clayey landslides. J. Appl. Geophys. 126, 98–115.

Glendinning, S., Helm, P.R., Roujainia, M., Stirling, R.A., Asquith, J.D., Hughes, P.N., Toll, D.G., Clarke, D., Powrie, W., Smethurst, J., Hughes, D., Harley, R., Karim, R., Dixon, N., Crosby, C., Chambers, J., Dijikstra, T., Gunn, D., Briggs, K., Muddle, D., 2005. Research-informed design, management and maintenance of infrastructure slopes: development of a multi-scalar approach. Int. Symp. Geohazards Geomech. 26, 012005.

Glendinning, S., Hughes, P., Helm, P., Chambers, J., Mendes, J., Gunn, D., Wilkinson, P., Uhlemann, S., 2014. Construction, management and maintenance of embankments used for road and rail infrastructure: Implications of weather induced pore water pressures. Acta Geotech. 9 (5), 799–816.

Griffiths, J.S., Stokes, M., Stead, D., Giles, D., 2012. Landscape evolution and engineering geology: results from IAEG Commission 22. Bull. Eng. Geol. Environ. 71, 605–636.

Gunn, D.A., Chambers, J.E., Uhlemann, S., Wilkinson, P.B., Meldrum, P.I., Dijkstra, T.A., Haslam, E., Kirkham, M., Wragg, J., Holyoake, S., Hughes, P.N., Hen-Jones, R., Glendinning, S., 2015. Moisture monitoring in clay embankments using electrical resistivity tomography. Constr. Build. Mater. 91 (1), 82–94.

Guzzetti, F., Peruccacci, S., Rossi, M., Stark, C.P., 2008. The rainfall intensity-duration control of shallow landslides and debris flows: an update. Landslides. 5, 3–17.

Hargreaves, G.H., Samani, Z.A., 1982. Estimating potential evapotranspiration. J. Irrig. Drain Engr. ASCE 108 (IR3), 223–230.

Hayley, K., Bentley, L.R., Gharibi, M., Nightingale, M., 2007. Low temperature dependence of electrical resistivity: implications for near surface geophysical monitoring. Geophys. Res. Lett. 34 (18).

Hendry, M.T., Macciotta, R., Martin, C.D., Reich, B., 2015. Effect of Thompson River elevation on velocity and instability of Ripley Slide. Can. Geotech. J. 52, 257–267.

Holmes, J., Chambers, J., Meldrum, P., Wilkinson, P., Boyd, J., Williamson, P., Huntley, D., Sattler, K., Elwood, D., Sivakumar, V., Reeves, H., Donohue, S., 2020. 4-Dimensional electrical resistivity tomography for continuous, near-real time monitoring of a landslide affecting transport infrastructure in British Columbia, Canada. Near Surf. Geophys. 18 (4).

Hugenschmidt, J., 2010. Geophysics and Non-destructive Testing for Transport Infrastructure, with Special Emphasis on Ground Penetrating Radar. PhD thesis. ETH Zurich.

Huntley, D., Bobrowsky, P., 2014. Surficial Geology and Monitoring of the Ripley Slide, near Ashcroft, British Columbia. Cananda. Geological Survey of Canada, Open File, p. 7531.

Huntley, D., Bobrowsky, P., Parry, N., Bauman, P., Candy, C., Best, M., 2017. Ripley Landslide: The Geophysical Properties of a Slow-Moving Landslide near Ashcroft, British Columbia. Geological Survey of Canada, Open File, p. 8062.

Huntley, D., Bobrowsky, P., Hendry, M., Macciotta, R., Elwood, D., Sattler, K., Best, M., Chambers, J., Meldrum, P., 2019. Application of multi-dimensional electrical resistivity tomography datasets to investigate a very slow-moving landslide near Ashcroft, British Columbia. Can. Landslides 16 (5), 1033–1042.

Huntley, D., Holmes, J., Bobrowsky, P., Chambers, J., Meldrum, P., Wilkinson, P., Donohue, S., Elwood, D., Sattler, K., Hendry, M., Macciotta, R., Roberts, N.J., 2020. Hydrogeological and geophysical properties of the very-slow-moving Ripley Landslide, Thompson River valley, British Columbia. Can. J. Earth Sci. 57 (12), 1371–1391. https://doi.org/10.1139/cjes-2019-0187.

Huntley, D., Bobrowsky, P., Macleod, R., Cocking, R., Joseph, J., Rotheram-Clarke, D., 2021. Field testing innovative differential geospatial photogrammetric monitoring technologies in mountainous terrain near Ashcroft, British Columbia. Can. J. Mount. Sci. 18 (1), 20.

IPCC, 2014. Climate change 2014: synthesis report. In: Core Writing Team, Pachauri, R. K., Meyer, L.A. (Eds.), Contribution of Working Groups I, II and III to the Fifth

Assessment Report of the Intergovernmental Panel on Climate Change. IPCC, Geneva, Switzerland, p. 151.
Krautblatter, M., Verleysdonk, S., Flores-Orozco, A., Kemna, A., 2010. Temperature-calibrated imaging of seasonal changes in permafrost rock walls by quantitative electrical resistivity tomography (Zugspitze, German/Austrian Alps). J. Geophys. Res. Earth Surf. 115 (F02003) https://doi.org/10.1029/2008JF001209.
Labuz, J.F., Zang, A., 2012. Mohr–Coulomb failure criterion. Rock Mech. Rock. Eng. 45, 975–979.
Lehmann, P., Gambazzi, F., Suski, B., Baron, L., Askarinejad, A., Springman, S.M., Holliger, K., Or, D., 2013. Evolution of soil wetting patterns preceding a hydrologically induced landslide inferred from electrical resistivity survey and point measurements of volumetric water content and pore water pressure. Water Resour. Res. 49, 7992–8004.
Lu, N., Godt, J.W., Wu, D.T., 2010. A closed-form equation for effective stress in unsaturated soil. Water Resour. Res. 46, W05515.
Macciotta, R., Hendry, M., Martin, D., Elwood, D., Lan, H., Huntley, D., Bobrowsky, P., Sladen, W., Bunce, C., Choi, E., Edwards, T., 2014. Monitoring of the Ripley Slide in the Thompson River Valley, B.C. Proceedings of Geohazards 6 Symposium. Kingston, Ontario, Canada.
Mallet, J.L., 1992. GOCAD: a computer aided design program for geological applications. In: Turner, A.K. (Ed.), Three-Dimensional Modeling with Geoscientific Information Systems. NATO ASI Series (Series C: Mathematical and Physical Sciences), 354. Springer, Dordrecht.
Marino, P., Peres, D.J., Cancelliere, A., Greco, R., Bogaard, T.A., 2020. Soil moisture information can improve shallow landslide forecasting using the hydrometeorological threshold approach. Landslides. 17, 2041–2054. https://doi.org/10.1007/s10346-020-01420-8.
Mattsson, L.-G., Jenelius, E., 2015. Vulnerability and resilience of transport systems – A discussion of recent research. Transp. Res. A Policy Pract. 81, 16–34.
Merritt, A.J., Chambers, J.E., Murphy, W., Wilkinson, P.B., West, L.J., Gunn, D.A., Meldrum, P.I., Kirkham, M., Dixon, N., 2014. 3D ground model development for an active landslide in Lias mudrocks using geophysical, remote sensing and geotechnical methods. Landslides 11 (4), 537–550.
Onda, Y., Tsujimura, M., Tabuchi, H., 2004. The role of subsurface water flow paths on hillslope hydrological processes, landslides and landform development in steep mountains of Japan. Hydrol. Process. 18, 637–650.
Perrone, A., Lapenna, V., Piscitelli, S., 2014. Electrical resistivity tomography technique for landslide investigation: A review. Earth Sci. Rev. 135, 65–82.
Piegari, E., Di Maio, R., 2013. Estimating soil suction from electrical resistivity. Nat. Hazards Earth Syst. Sci. 2369–2379.
Porter, M., Savigny, K., Keegan, T., Bunce, C., MacKay, C., 2002. Controls on stability of the Thompson River landslides. In: Proceedings of the 55th Canadian Geotechnical Conference: Ground and Water – Theory to Practice, Canadian Geotechnical Society, pp. 1393–1400.
Samani, Z., 2000. Estimating solar radiation and evapotranspiration using minimum climatological data. J. Irrig. Drain. Eng. 126 (4), 265–267.
Samoüelian, A., Cousin, I., Tabbagh, A., Bruand, A., Richard, G., 2005. Electrical resistivity survey in soil science: a review. Soil Tillage Res. 83, 173–193.
Sattler, K., Elwood, D., Hendry, M.T., Huntley, D., Holmes, J., Wilkinson, P.B., Chambers, J., Donohue, S., Meldrum, P.I., Macciotta, R., Bobrowsky, P.T., 2021. Quantifying the contribution of matric suction on changes in stability and displacement rate of a translational landslide in glaciolacustrine clay. Landslides. https://doi.org/10.1007/s10346-020-01611-3.
Smethurst, J.A., Smith, A., Uhlemann, S., Wooff, C., Chambers, J., Hughes, P., Lenart, S., Saroglou, H., Springman, S.M., Löfroth, Hughes, D., 2017. Current and future role of instrumentation and monitoring in the performance of transport infrastructure slopes. Q. J. Eng. Geol. Hydrogeol. 50, 271–286.
Springman, S., Teysseire, M.P., Jommi, C., 2003. Instabilities on moraine slopes induced by loss of suction: a case history. Geotechnique. 53 (1), 3–10.
Stark, T.D., Eid, H.T., 1994. Drained residual strength of cohesive soils. J. Geotech. Eng. ASCE 120 (5), 856–871.
Supper, R., Ottowitz, D., Jochum, B., Kim, J.-H., Römer, A., Baron, I., Pfeiler, S., Lovisolo, M., Gruber, S., Vecchiotti, F., 2014. Geoelectrical monitoring: an innovative method to supplement landslide surveillance and early warning. Near Surf. Geophys. 12, 133–150.
Thornton, J.M., Mariethoz, G., Brunner, P., 2018. A 3D geological model of a structurally complex Alpine region as a basis for interdisciplinary research. Sci. Data 5 (180238).
Toll, D.G., Lourenco, S.D.N., Mendes, J., Gallipoli, D., Evans, F.D., Augarde, C.E., Cui, Y. J., Tang, A.M., Rojas, J.C., Pagano, L., Mancuso, C., Zingariello, C., Tarantino, A., 2011. (2011) Soil suction monitoring for landslides and slopes. Q. J. Eng. Geol. Hydrogeol. 44, 1–13. https://doi.org/10.1144/1470-9236/09-010.
Tye, A.M., Kessler, H., Ambrose, K., Williams, J.D.O, Tragheim, D., Scheib, A., Raines, M., Kuras, O., 2011. Using integrated near-surface geophysical surveys to aid mapping and interpretation of geology in an alluvial landscape within a 3D soil-geology framework. Near Surf. Geophys. 9 (1), 15–31.
Uhlemann, S., Chambers, J., Wilkinson, P., Maurer, H., Merritt, A., Meldrum, P., Kuras, O., Gunn, D., Smith, A., Dijkstra, T., 2017. Four-dimensional imaging of moisture dynamics during landslide reactivation. J. Geophys. Res. Earth Surf. 122 (1), 398–418.
Wasowski, J., Bovenga, F., 2022. Chapter 11 - Remote sensing of landslide motion with emphasis on satellite multi-temporal interferometry applications: an overview. Landslide Hazards, Risks, and Disasters 365–438.
Waxman, M.H., Smits, L.J.M., 1968. Electrical conduction in oil-bearing sands. Soc. Pet. Eng. J. 8, 107–122.
Whiteley, J., Chambers, J., Uhlemann, S., Wilkinson, P., Kendall, J., 2019. Geophysical monitoring of moisture-induced landslides: a review. Rev. Geophys. 57 (1), 106–145.
Wilkinson, P.B., Chambers, J.E., Meldrum, P.I., Gunn, D., Ogilvy, R.D., Kuras, O., 2010. Predicting the movements of permanently installed electrodes on an active landslide using time-lapse geoelectrical resistivity data only. Geophys. J. Int. 183, 543–556.
Wilkinson, P., Chambers, J., Uhlemann, S., Meldrum, P., Smith, A., Dixon, N., Loke, M. H., 2016. Reconstruction of landslide movements by inversion of 4-D electrical resistivity tomography monitoring data. Geophys. Res. Lett. 43 (3), 1166–1174.
Wu, Y., Hubbard, S., Ulrich, C., Wullschleger, S., 2013. Remote monitoring of Freeze-Thaw transitions in arctic soils using the complex resistivity method. Vadose Zone J. 12 https://doi.org/10.2136/vzj2012.0062.
Yao, W., Li, C., Zhan, H., Zeng, J., 2019. Time-dependent slope stability during intense rainfall with stratified soil water content. Bull. Eng. Geol. Environ. 78, 4805–4819.
Zhang, F., Wang, G., 2018. Effect of irrigation-induced densification on the post-failure behavior of loess flowslides occurring on the Heifangtai area, Gansu, China. Eng. Geol. 236.